

Project: **989**

Project title: **Long transient simulations of the last deglaciation (last 30,000 years) and the development of lithosphere and ice sheet models in the framework of PalMod Working Group 1, Physical System**

Project lead: **Gerrit Lohmann**

Report period: **2019-01-01 to 2019-12-31**

We report on our modeling efforts on Mistral during the first 10 months of the allocation period 2019, covering proposed simulations with MPI-ESM, PISM, ISSM, VILMA, CCLM, and AWI-ESM.

The GFZ (PalMod WP1.1-TP5 and WP1.2-TP4) utilized VILMA to reconstruct the glacial-isostatic adjustment (GIA) as the solid-Earth component in PalMod. Using model ensembles the variability of relative sea level and paleo-topography during the last glacial cycle was analyzed under a number of aspects. Several 1D and 3D model ensembles with different solid-earth and glacial-history parameterizations were generated. (1) We continued our 3D model runs. We created sets of 3D viscosity-structures and applied them for 3D model runs. The structure sets are derived from seismic tomography models and geodynamic constraints and differ in lithospheric thickness and lateral and radial viscosity distribution. (2) Based on 3D Earth structures, we created derived 1D Earth structures and applied them for 1D model runs in order to compare the model results and to analyze the effect of lateral viscosity variations. Derived 1D Earth structures include “global mean” structures as well as “locally adapted” structures that use the local structure as global 1D structure in order to analyze the effect in a selected region. (3) We validated the reconstructions of the late-glacial relative sea-level with sea-level indicators. Figure 1 summarizes the Earth structure, model results and validation with sea-level data for a selected model setup.

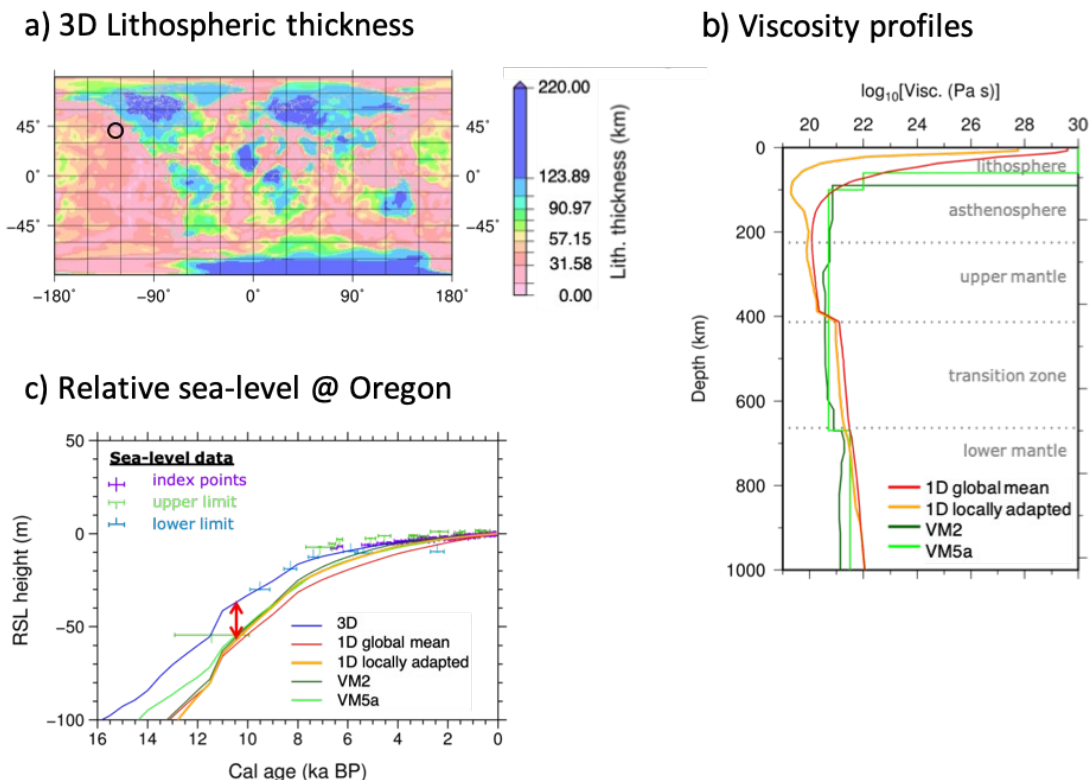


Figure 1: (a) Lithospheric thickness of a selected 3D Earth structure. (b) Viscosity profiles of derived “global mean” and “locally adapted” 1D Earth structure. The locally adapted structure represents the local viscosity structure of the Central Oregon Coast (black circle in (a)). As comparison also Peltier’s VM2 and VM5a 1D Earth structures are shown. (c) Relative sea-level reconstruction at the Central Oregon Coast for the 3D model, the derived 1D “global mean” model, the derived 1D “locally adapted” model and Peltier’s 1D VM2 and VM5a models. Sea-level indicators are separated in index points (purple), upper limit (green) and lower limit (blue) data.

At MPI-Met, ocean bathymetry, land orography, land-sea mask and river-routing are now interactively calculated in the model. These features have been extensively tested in deglacial simulations with prescribed ice sheets and topography based on reconstructions (ICE-6G and GLAC1D). The results look reasonable and support the hypothesis, that the Younger Drays could be caused by changing river routing, deflecting the meltwater discharge from the Mississippi to the Arctic.

Another extension of the system are interactive icebergs, which are based on a new developed module inside MPIOM. First results from a set of ongoing sensitivity experiments show, that the inclusion of interactive icebergs has a strong effect on the sensitivity of the AMOC to prescribed meltwater/iceberg input, compared both to a point source input as well as to the often used latitude belt input. Icebergs are now included in the fully coupled MPI-M fully coupled model system as well.

One focus of the work was the development of the fully coupled model system MPI-ESM-CR/PISM/VILMA with interactive land-sea mask (see Figure 2). The system was extended to include the southern hemisphere ice sheet and icebergs. The tuning process for this coupled model is ongoing in accelerated simulations. The originally planned transient synchronous deglacial simulations with the fully coupled model of WP1.3 could not be performed in 2019 due to parental leave of the responsible scientist. They will be performed in early 2020.

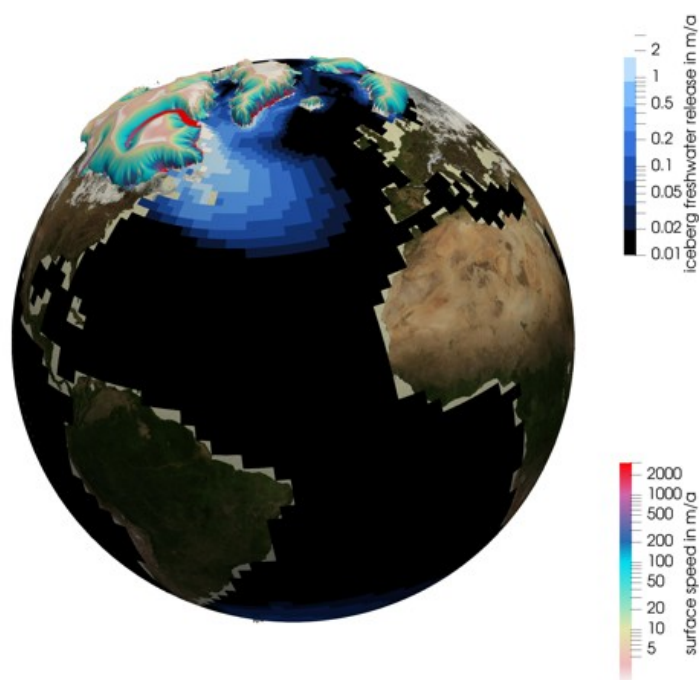


Figure 2: The distribution of the meltwater release from icebergs during a simulated Heinrich event from the fully coupled MPI-M model system.

At the AWI the fully coupled AWI-ESM/PISM climate-ice-sheet-setup has been employed for transient coupled ice sheet / climate simulations spanning the time period around the Last Glacial Maximum (LGM). In order to facilitate a better understanding of the reaction of the coupled system to meltwater discharge during transient simulations the model AWI-ESM was furthermore employed based on the ICE6G topography for various studies that tested the sensitivity of the climate system to location and strength of freshwater forcing to the ocean, with and without changing atmospheric carbon dioxide. It has been shown that the 50-60°N ice rafted debris belt is the most efficient way to bring the AMOC into a weak state, and that a hosing between 0.10-0.15 Sv leads to a weak AMOC that is subsequently able to overshoot. The results have furthermore highlighted that increasing carbon dioxide is able to accelerate AMOC overshoot (Figure 3a). Model development has continued by improving subsystems of the climate system and speed of model execution towards achieving the throughput necessitated in PalMod2. A milestone has been finalization of version 2 of the FESOM,

that has been shown to provide high model throughput and scalability (Koldunov et al., 2019) in the coupled AWI-ESM model setup (Sidorenko et al., in press). To allow transition from FESOM1.4 to FESOM2 in the AWI-ESM glacial model states have been compared for both model versions. The AMOC shows comparable behavior of the LGM, albeit being stronger in the setup with FESOM2 linked to an updated mixing scheme. The LakeCC model (Hinck et al., in review) was developed to identify lake basins within the paleo-topography (Figure 3d). Pro-glacial lakes act as a freshwater-buffer in the climate system, but also pose marine-like boundary conditions to the continental margins of ice-sheets. In a first study the model was applied to ice and paleo-topography reconstructions of North America. In a next step the LakeCC model is coupled to an ice-sheet model and thereafter included into the fully coupled AWI-ESM climate system.

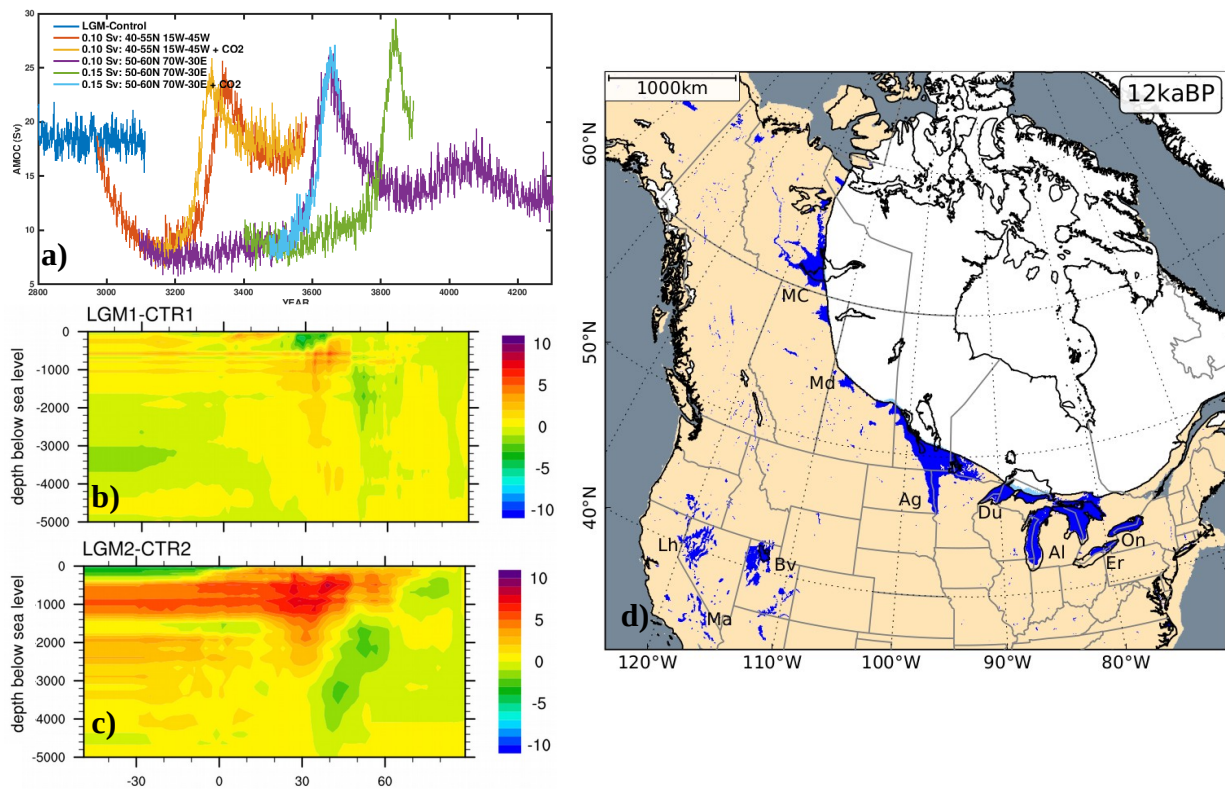


Figure 3: (a) Sensitivity of the AMOC to the strength of hosing with and without changing the concentration of carbon dioxide. (b,c) Comparison of difference in AMOC strength (glacial minus pre-industrial) for the AWI-ESM with FESOM1.4 (b) and FESOM2 (c). (d) Reconstruction of pro-glacial lakes in North America at 12 ka BP using the LakeCC model (Hinck et al., in review). Lake names are abbreviated as follows: Ag - Agassiz, Al - Algonquin, Bv - Bonneville, Du - Duluth, Er - Erie, Lh - Lahontan, MC- McConnell, Ma - Manly, Md - Meadow, On - Ontario.

In 2019 the COSMO-CLM was employed by KIT in the framework of regional ice sheet modelling for the CORDEX-Arctic region for the missing 45 years of MPI-ESM pre-industrial and LGM climate conditions (AWI, T31) provided in the end of 2018. Results for precipitation and surface mass balance are presented in Figure 4. Furthermore, the model was driven with a new MPI-ESM data set (T31) provided by AWI. Due to the low resolution of MPI-ESM data a two-step-nesting was needed (0.88°; 0.22°). However, due to technical problems for the new data set only 5 years of PI conditions and 14 years LGM climate conditions were simulated on 0.22°. Additionally for the CORDEX-Europe region the model was driven by a new MPI-ESM data set on T31 resolution provided by MPI. Simulations were performed on 0.44° resolution for pre-industrial and mid-holocene climate conditions for 30 years each.

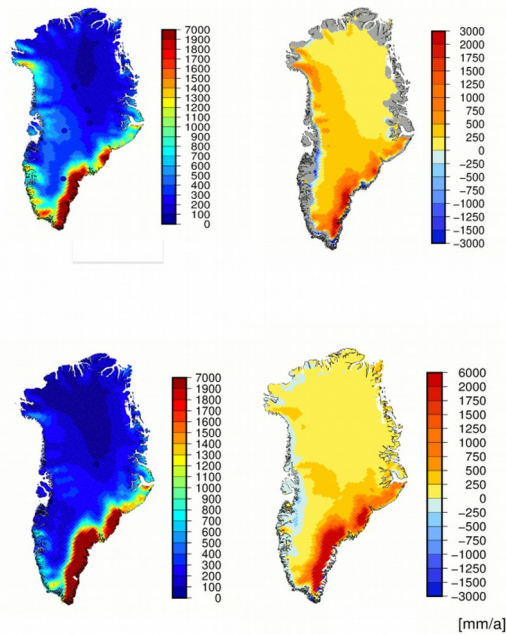


Figure 4: Example for COSMO-CLM 0.22° simulations driven with MPI-ESM data of 50 years. Top: PI average for 1850-1900. Ice cores: DYE-3, Milcent, Crete, GRIP, NGRIP (Andersen et al., 2006). Bottom: LGM average for 50 years including GRIP data (Alley, 2000). Left: precipitation, Right: surface mass balance.

In 2019 the 3d ocean forcing parameterization according to the [CMIP6/ISMIP6 protocol](#) has been implemented in PISM (v1.1) by AWI (PalMod WP1.2-TP1). In addition, our glacial index method for atmosphere and ocean forcing has been adapted for the new parameterization and PISM version to run long ISM spin-ups with paleo-climatic forcing. Results of previous spin-up simulations have been published within the context of ISMIP6/initMIP-Antarctica (Seroussi et al., 2019). First results of our new 8 km resolution PISM set-up with steady present-day climate have been submitted to ISMIP6. We have worked again on a number of bug fixes related mainly to model restarts and reproducibility in PISM. The thermal present-day state of the Antarctic ice sheet from PISM (16 km resolution) has been used to initialize the Ice Sheet System Model (ISSM) in a high-resolution regional set-up for the Recovery Glacier, Antarctica. This set-up has been used to infer basal properties that cannot be observed directly by inverse modelling (Figure 5).

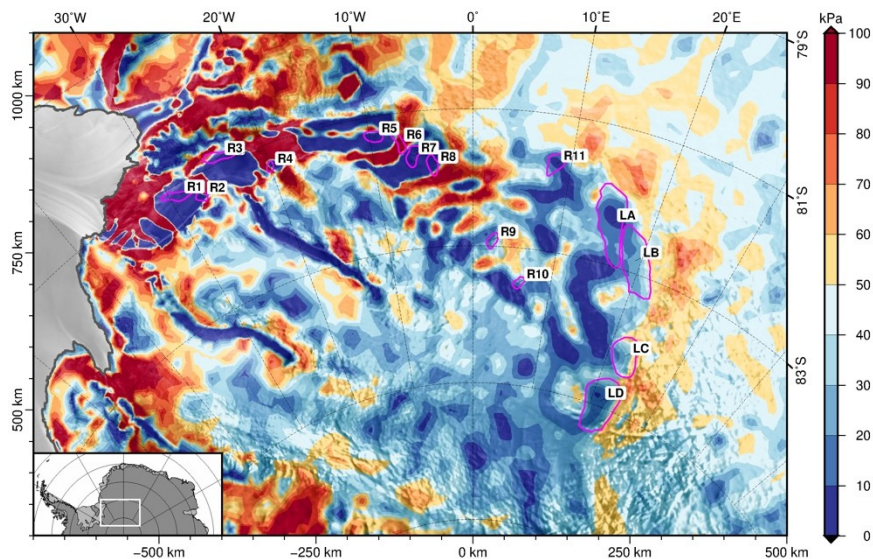


Figure 5: Inferred basal drag in the Recovery Glacier based on inverse modelling with ISSM and forward modelling with PISM. Proposed sub-glacial lake outlines are shown in magenta with superimposed labels according to previous studies.

References:

- Gowan, E. J., Tregoning, P., Purcell, A., Montillet, J.-P., and McClusky, S. (2016). A model of the western Laurentide Ice Sheet, using observations of glacial isostatic adjustment. *Quaternary Science Reviews*, 139, 1-16. doi:10.1016/j.quascirev.2016.03.003
- Hinck, S. , Gowan, E. J. , and Lohmann, G. (in review). LakeCC: a tool for efficiently identifying lake basins with application to paleo-geographic reconstructions of North America. In revision for *Journal of Quaternary Science*.
- Koldunov, N. V., Aizinger, V., Rakowsky, N., Scholz, P., Sidorenko, D., Danilov, S., and Jung, T. (2019). Scalability and some optimization of the Finite-volume Sea ice–Ocean Model, Version 2.0 (FESOM2). *Geoscientific Model Development*, 12, 3991-4012. doi:10.5194/gmd-12-3991-2019
- Seroussi, H., Nowicki, S., Simon, E., Abe-Ouchi, A., Albrecht, T., Brondex, J., Cornford, S., Dumas, C., Gillet-Chaulet, F., Goelzer, H., Golledge, N. R., Gregory, J. M., Greve, R., Hoffman, M. J., Humbert, A., Huybrechts, P., Kleiner, T., Larour, E., Leguy, G., Lipscomb, W. H., Lowry, D., Mengel, M., Morlighem, M., Pattyn, F., Payne, A. J., Pollard, D., Price, S. F., Quiquet, A., Reerink, T. J., Reese, R., Rodehacke, C. B., Schlegel, N.-J., Shepherd, A., Sun, S., Sutter, J., Breedam, J. V., van de Wal, R. S. W., Winkelmann, R., and Zhang, T. (2019). initMIP-Antarctica: an ice sheet model initialization experiment of ISMIP6, *The Cryosphere*, 13, 1441–1471. doi:10.5194/tc-13-1441-2019
- Sidorenko, D., Goessling, H. F., Koldunov, N., Scholz, P., Danilov, S., Barbi, D., Cabos, W., Gurses, O., Harig, S., Hinrichs, C., Juricke, S., Lohmann, G., Losch, M., Mu, L., Rackow, T., Rakowsky, N., Sein, D., Semmler, T., Shi, X., Stepanek, C., Streffing, J., Wang, Q., Wekerle, C., Yang, H., and Jung, T (2019). Evaluation of FESOM2.0 coupled to ECHAM6.3: Pre-industrial and HighResMIP simulations. *Journal of Advances in Modeling Earth Systems (in press)*.
- Ziemen, F., Kapsch, M.-L., Klockmann, M., and Mikolajewicz, U. (2019). Heinrich events show two-stage climate response in transient glacial simulations. *Climate of the Past*, 15, 153-168. doi:10.5194/cp-15-153-2019

Project: **1030**

Project title: **PalMod WG2**

Project lead: **Victor Brovkin**

Report period: **2019-01-01 to 2019-12-31**

PalMod is a BMBF-funded project focused on understanding earth system dynamics and variability during the last glacial cycle. The first phase of PalMod ran from 2015-08-01 to 2019-07-31 and focused on the time from the Last Glacial Maximum to the present. The second project phase runs from 2019-10-01 to 2022-09-30 and will revisit the deglaciation, but also investigate the glacial inception and the strong variability during Marine Isotope Stage 3.

WG2 of PalMod aims at understanding and quantifying feedbacks between biogeochemistry and climate during glacial cycles. Three work packages are focusing on the marine carbon cycle, terrestrial processes, and the CH₄ cycle. During the first project phase, an additional fourth work package investigated the dust cycle. Scientific challenges include reproducing the glacial CO₂ cycle with comprehensive ESMs, understanding of rapid changes in atmospheric greenhouse gas concentrations during abrupt climate changes, and reconstructing the atmospheric lifetime of CH₄ using a coupled atmospheric chemistry model.

PalMod WG2 contains work packages WP2.1 "Marine carbon cycle", WP2.2 "Terrestrial carbon cycle", WP2.3 "Methane cycle", and WP2.4 "Dust cycle". During the reporting period all work packages requested computation time from DKRZ, but WP2.4 will not request computation time for 2020 as it was not prolonged.

Internal reallocation of computation time

Of the 398940 node-h requested by WG2 for 2019, only 144711, roughly 40%, were actually granted. This reduction by 60% led to severe cuts in the experiments we were able to perform. Especially the transient production experiments for publication purposes were strongly delayed, as we could not foresee whether sufficient computational resources would be available. Fortunately, we managed to conduct some simulations using the remaining computation time from other projects. Specifically WP2.1 used (by October 2019) 10845 node hours from WG4/bk0993, and 17157 node hours from bm0976 (CRESCENDO), while WP2.2 and 2.3 used 21581 node hours from mj0060 (MPI-M) and 1400 node hours from bm0903.

In addition, we have recently been granted some 48000 node-h from Palmod WG1, allowing us to finish some crucial transient experiments before the end of this year.

Report 2019

WP 2.1 "Marine carbon cycle", CAU Kiel

In 2019, our group has started to work on the setup and initialization of MPI-ESM including HAMOCC in the LGM. However, the envisioned transient simulations of the last deglaciation were not yet started due to unforeseen delays and technical difficulties with respect to the coupled MPI-ESM model setup with interactive land-sea mask for the LGM. The LGM setup is now available and running, and the very limited remaining computing time in 2019 will be used to further prepare and improve an LGM time slice experiment with MPI-ESM and HAMOCC, which will serve as an initial condition for the transient simulations of the deglaciation, which we are now planning to run in 2020.

While the LGM setup was not yet available, and in preparation for later inception simulations, MPI-ESM in coarse resolution (CR, T31GR30) as well as low resolution (LR, T63GR15) was used to investigate differences between Holocene and Eemian climate (prescribing orbital parameter changes). A preliminary analysis of the CR model results shows, for example, that the annual cycle amplitude in the Niño3 region is strengthening from early to late interglacials (i.e, both in the Eemian and Holocene; Fig. 1). Moreover, the seasonal cycle phase is shifted, where the spring/summer temperature maximum occurs earlier in the year for late interglacials. These results are consistent with a previous study based on the Kiel Climate Model (Khon et al., 2018, GRL). However, the LR simulations show a smaller effect on the amplitude, and different phase shifts.

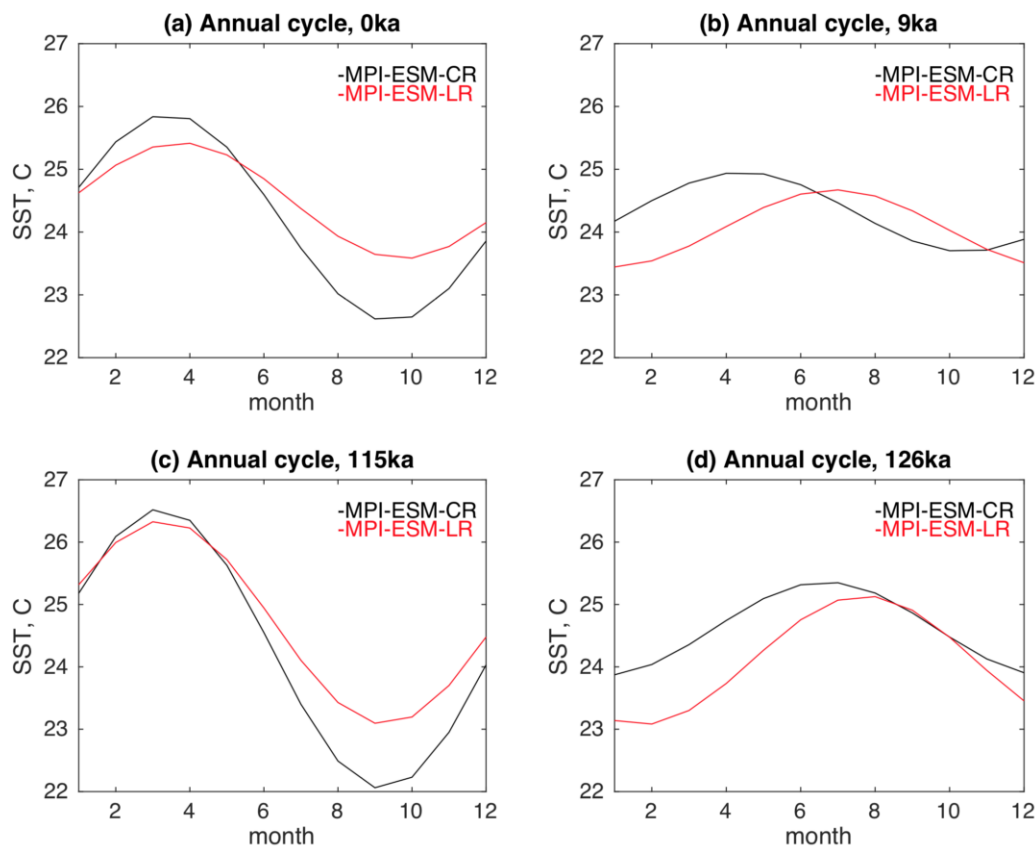


Figure 1: Annual cycle of SST averaged over Niño3 region for the Holocene (a, b) and Eemian (c, d) simulated by MPI-ESM-CR and MPI-ESM-LR.

WP 2.1 “Marine carbon cycle“, MPI-M

1 Evaluation of ^{13}C module in present-day ocean

We tested two parameterisations for the biological fractionation factor during photosynthesis: one depends on the seawater temperature and pCO_2 (Popp et al., 1989), the other is a function of seawater temperature, pCO_2 , as well as phytoplankton growth rate (Laws et al. 1995). Based on the comparison to observed $\delta^{13}\text{C}_{\text{POC}}$, shown in Fig. 2a-2c, the former parameterisation has a better performance. The $\delta^{13}\text{C}_{\text{DIC}}$ distribution (Fig. 2d-2f), however, differs little between the two parameterisations. We also compared the simulated $\delta^{13}\text{C}$ Suess effect, the intrusion of isotopically light anthropogenic carbon into the ocean, to the estimates from Eide et al. (2017). The major feature of the data, greater Suess effect at depth of the subtropical regions, is reproduced well in the model. However, regional disagreements exist between model and data. With the comparison of simulated CFC11 to data (not shown), we are able to attribute the differences to the biases in ocean physical states and to those in biogeochemical processes. Based on the above simulations and analysis, we are currently preparing a manuscript.

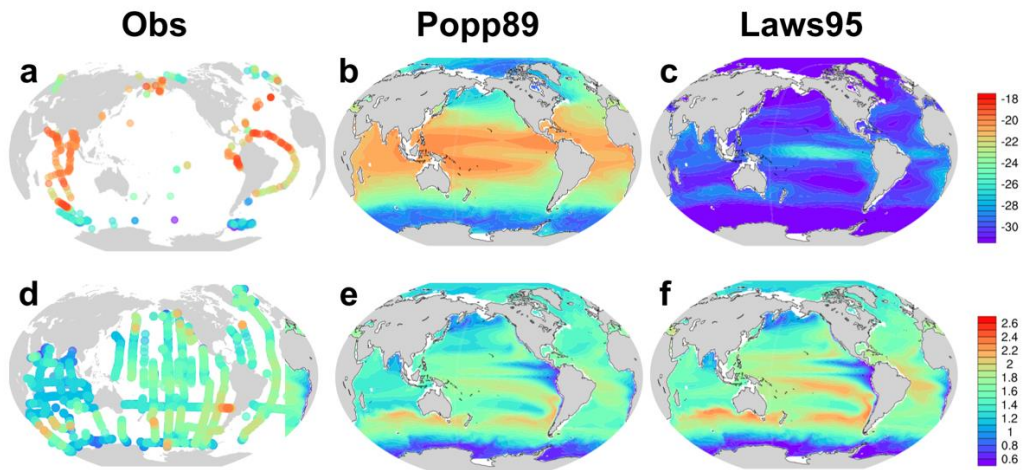


Figure 2. Upper row: the surface 100m-averaged $\delta^{13}\text{C}_{\text{POC}}$ in (a) observation, (b) the simulation with the biological fractionation factor parameterisation from Popp et al. (1989), and (c) the simulation with the biological fractionation factor parameterisation from Laws et al. (1995). Lower row, as the upper row, but for $\delta^{13}\text{C}_{\text{DIC}}$.

2 LGM time-slice simulations

We carried out simulations to investigate the quantitative impact of different LGM AMOC states and that of an increased export production in the SO on the oceanic $\delta^{13}\text{C}$ distribution.

2.1 Impact of different LGM AMOC states

To vary the LGM AMOC states, we used two approaches, respectively. First, we applied air-sea freshwater flux adjustment to modify the meridional salinity gradient directly. Second, we applied adjustments of the air-sea net heat flux to increase ice formation in the SO and thereby increase AABW production.

We added freshwater at the sea surface of the North Atlantic and subtracted the same amount of freshwater at the surface of the South Atlantic. We tested different areas to apply the freshwater fluxes: 45-65 °N, 50-70 °N and 50-80 °N in the NA; 50-90 °S and the shelf area (shallower than 1000m) in the SA; and we tested different freshwater amounts (0.2, 0.25, 0.3 and 0.4 Sv). We find that as the boundary between the upper NADW cell and the lower AABW cell of AMOC shoals and the NADW strength decreases (Fig. 3), positive $\delta^{13}\text{C}$ anomalies are mainly confined to the upper 2000m and negative $\delta^{13}\text{C}$ anomalies occurs below 2000m, which is seen in proxy data.

We removed net heat at the sea surface of the SO and added the same amount of net heat at the surface of the rest area of the ocean. We tested different areas to subtract the net heat fluxes, as well as different values of the net heat flux change. Preliminary results show that when using a net-heat flux of 25 Wm^{-2} , the AABW production is noticeably increased, however, the $\delta^{13}\text{C}$ anomalies in the NA at depth is slightly decreased due to increased ventilation (not shown).

2.2 Impact of an increased export production in the SO

In the current MPI-ESM-CR model set-up, phytoplankton growth in the SO is not limited by iron. Thus, to increase the export production in the SO, we doubled the phytoplankton growth rate in this region. Under an increased export production in the SO and a shallow, weak AMOC, the simulated $\delta^{13}\text{C}$ anomalies are in better agreement with proxy data (Fig. 3).

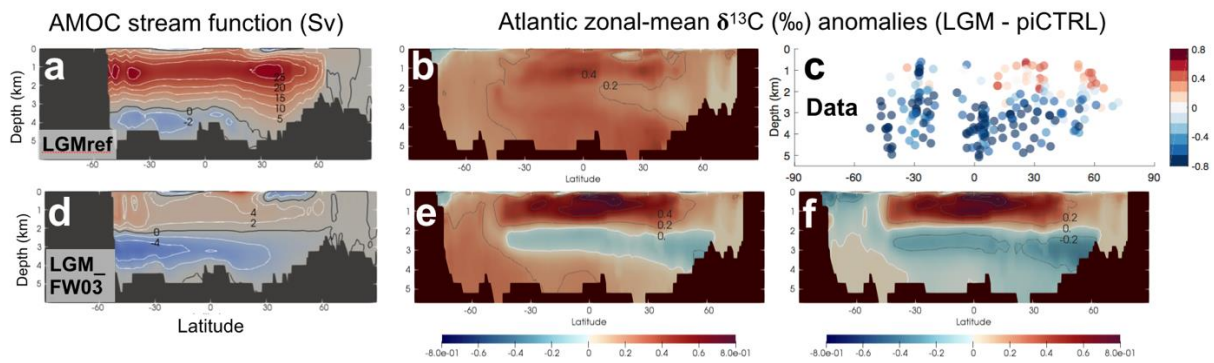


Figure 3. *a* and *b*: AMOC stream function (Sv) and Atlantic zonal-mean $\delta^{13}\text{C}$ (permil) anomalies between LGM and pre-industrial state for the LGM reference run. *c*: Proxy data from Peterson et al. (2014). *d* and *e*: as *a* and *b*, but for the LGM simulation with a surface freshwater adjustment of 0.3 Sv. *f*: as *e*, but the doubled phytoplankton growth in the Southern Ocean.

3 Implications of dynamical riverine fluxes in the ocean

Riverine inputs of carbon, nutrients and alkalinity were added to the ocean biogeochemistry component of the MPI-ESM component HAMOCC. These include a new tracer for terrestrial dissolved organic matter (tDOM), which carries larger fractions of carbon in relation to nutrients. The implications of riverine exports were tested in the GR15 resolution in a model setup forced with pre-industrial atmospheric conditions. The model was also tested for dynamic changes of the riverine fluxes in simulations performed over a historical time-period (1850-2010). These simulations show that changes in nutrient supplies affect the global oceanic net primary production at the global scale, even for this short time period.

In order to account for changes in riverine fluxes and of river mouths locations from the LGM to the Holocene, a module is being implemented which will quantify terrestrial exports and the changes in river mouth locations for every 10 model years.

WP2.2 “Terrestrial Carbon Cycle”, MPI-M

In 2019 WP2.2 mainly investigated carbon cycle changes arising as a consequence of changes in the land-sea mask during deglaciation, using a transient model experiment performed together with WP2.3. At the LGM, land C storage outside the PI land-sea mask, i.e. on the continental shelves was 123 PgC. At 10 ka BP, this was still some 43 PgC. We were able to close the carbon cycle for the case where land was flooded by passing C to the ocean C cycle model, while we will address the reverse case in 2020.

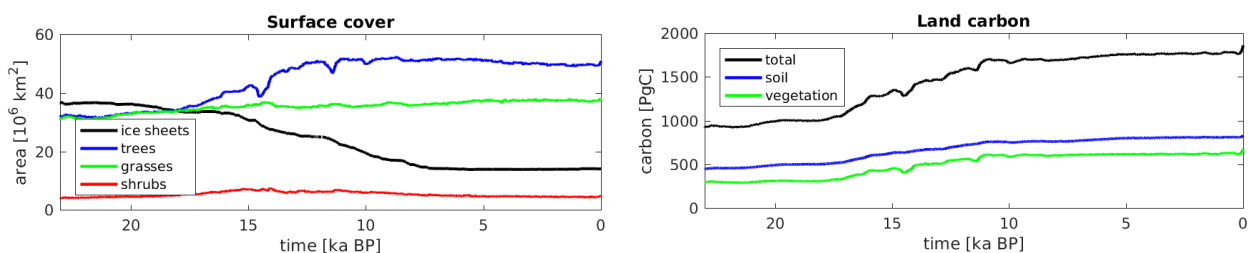


Figure 4: Transient change in surface cover (left) and land C pools (right) from LGM to PI.

As ice cover shrinks during the deglaciation (Figure 4, left), tree cover expands, leading to a strong increase in land carbon. Land cover by grasses and shrubs, however doesn't change very much, although the areas change, i.e. formerly grass covered areas in the high latitudes are invaded by trees, while formerly ice-covered areas are taken over by grasses. This increases the total terrestrial carbon stock by roughly 800 PgC, with the increases equally distributed between soil and vegetation carbon (Fig. 4, right). However, C stocks in the present model set up are substantially larger than in previous model versions, and investigations with regard to the cause of these differences are still ongoing.

Furthermore, we investigated the long-term effect of the presence of humans on the carbon cycle with regard to fires, as fire probabilities increase if humans are present, by applying a recently developed data set of human population. The latter exists for the last 10000 years, but we only investigated the last 5000 years.

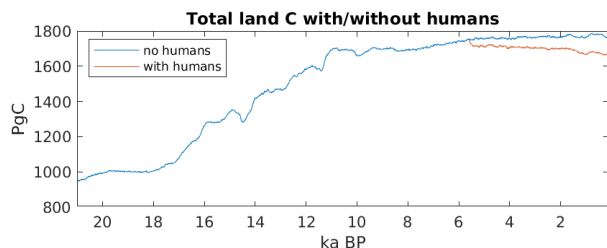


Figure 5: Total land C storage with and without considering human fire ignitions.

We find that the presence of humans decreases the total land C storage by some 100 PgC in the PI situation (Figure 5), with tree cover decreasing and grass cover increasing as the human population increases.

#cores ECHAM	#cores MPIOM	#nodes compute2	runtime (s/yr)	node-h/yr	SYPD
192	24	6	251	0.42	343.63
288	36	9	188	0.47	459.45
384	48	12	161	0.54	535.13
576	72	18	136	0.68	633.80
576	120	20	129	0.72	667.50

Table 1: Runtime and computational cost per model year, depending on number of nodes used

Finally, WP 2.2 conducted a model performance assessment to determine optimal model configurations with regard to model parallelisation and turnover. We found that we could nearly double the model turnover in terms of simulated years per day (SYPD) by better allocating computational resources, though at some cost in terms of node-hours. Table 1 does not, however show the full computational cost, as the scaling tests were performed without the HAMOCC model and without the land-sea mask change scripting, which also consume significant resources.

WP 2.3 “Methane cycle” (MPI-M)

In 2018 we assessed the methane cycle over the deglaciation. We performed transient experiments from LGM to PI, as well as a number of short AMOC perturbation experiments for the Bølling-Allerød and Younger Dryas transitions. These model experiments were the first experiments that were performed with a dynamically changing parameterisation of the methane sink, as developed by MPI-C and integrated in MPI-ESM.

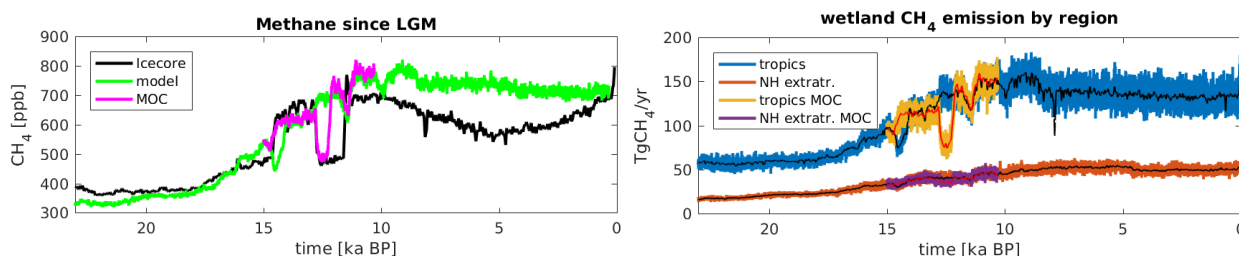


Figure 6: (left) Atmospheric methane concentration as simulated by MPI-ESM (green) against ice-core reconstruction (black). AMOC perturbation (magenta) allows reproduction of B/A-YD transition magnitude. (right) Wetland methane emissions from tropics (blue) and NH extratropics (brown). AMOC perturbation (red) leads to strong decrease in tropical emissions.

Atmospheric methane, as determined by MPI-ESM (Fig. 6, left) is close to ice core reconstructions for much of the deglaciation, though concentrations during the Holocene are somewhat higher than in ice cores. In unperturbed experiments the Bølling-Allerød and Younger Dryas are not reproduced, as a collapse of the AMOC leads to a NH cooling right after the start of the B/A. In AMOC perturbation experiments, however, it is possible to reproduce the timing and magnitude of the B/A-YD transition, though we cannot yet reproduce the length of the Younger Dryas. The latter would have required a larger number of AMOC perturbation experiments, which we will perform later this year.

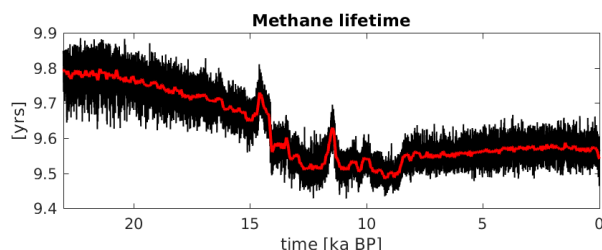


Figure 7: Methane lifetime in from LGM to PI

In line with expectations and time slice experiments, the bulk of the methane emissions originate in tropical wetlands (Fig. 6, right), and the emissions from these decrease strongly during the induced AMOC collapse. The lifetime of methane, on the other hand, decreases slightly from LGM to early Holocene (Fig. 7), increasing thereafter.

A publication of the results is in preparation, however model results are not quite publication ready, as some code bugs were found, a repeat experiment will be required before publication.

WP 2.3 “Methane cycle” (MPI-C)

Atmospheric oxidative capacity and climate variations

Within the project year 2019, we have completed numerical experiments on past atmosphere oxidative capacity (the main driver of atmospheric CH₄ removal) with the ECHAM5/MESy Atmospheric Chemistry (EMAC) AC-GCM driven by MPI-ESM-P lgm_r1i1p1-P experiment (Giorgetta et al., 2013) output for the past climate conditions. We focussed on (1) detailed investigation of the changes to lightning nitrogen oxide source (LNO_x), (2) improved estimates of the trace gas emission sources and (3) assessment of the uncertainties associated with complexity of chosen chemical kinetics mechanism.

The ensemble of LNO_x parameterisations in EMAC generally predicts a perceptible reduction of this source in the Last Glacial Maximum (LGM) as compared to the present day (PD) conditions (see Fig. 8 below). However, two of the parameterisations, viz. PaR_T and FinIF, simulate the largest negative-over-land and positive-over-ocean changes in LNO_x. Whereas PaR_T result is physically plausible owing to much stronger sensitivity of LNO_x to convection over land, the result of FinIF parameterisation (using convective ice flux as a proxy for lightning activity) is rather difficult to interpret. Our further work will be focused on calibrating each parameterisation for the PD conditions using available global observation proxies (flash counts, tropospheric ozone abundance). Calibrated parameterisations will lead to more certain estimates about atmospheric oxidative capacity changes, as LNO_x is the main driver of the latter in pre-industrial times.

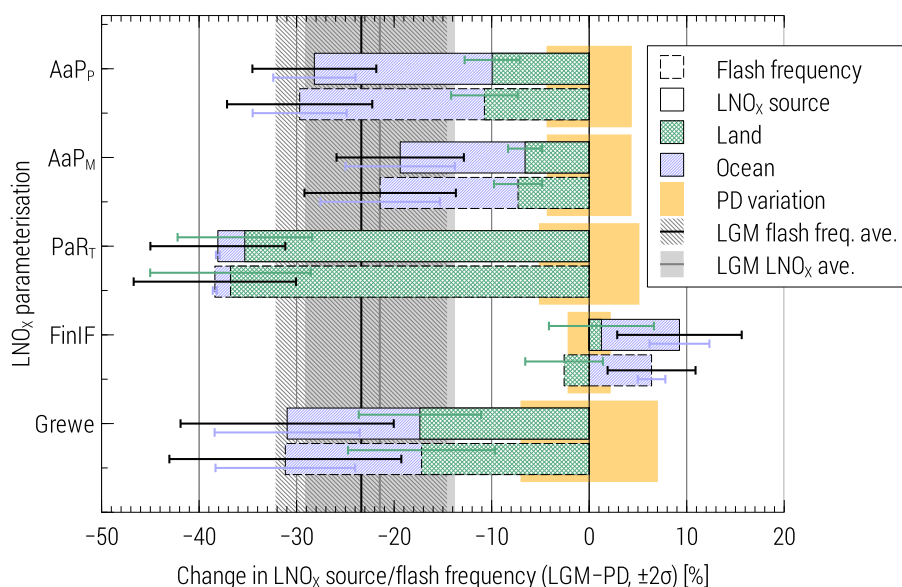


Figure 8: LGM–PD relative change of the lightning flash frequency and LNO_x source simulated by five different parameterisations in EMAC. Error bars/shaded areas denote variation in annual means. Grey shaded areas denote the ensemble “best guess” about the LNO_x source in the LGM.

A series of sensitivity simulations were performed in order to amend the trace gas emission setup in EMAC for the LGM conditions. In particular, we have calibrated the biomass burning (BB) emissions calculated with BIOBURN submodel using MPI-ESM fire proxy. EMAC predicts CH₄ BB emissions reduction within the range of 84% to 42% of the PD estimates, which is consistent with the range in previous works (see refs. in, e.g., Hopcroft et al., 2017). In comparison, a somewhat more moderate reduction in emissions of biogenic C (to 73%–81%, mostly isoprene, C₅H₈) and NO_x (to 80%–69%), but not for NH₃ (to 18%– 7%) was obtained. Overall, in the absence of anthropogenic emissions, such reduction in natural sources’ strength increases the decisive role of the LNO_x source in setting atmospheric oxidative capacity in past atmospheres.

Last but not least, we have performed control simulations with the most comprehensive kinetic chemistry mechanism MOM (Mainz Organics Mechanism, Sander et al. (2019), ~2000 reactions of ~800 species), which is factor ~4 more resource-intensive than the MIM (Mainz Isoprene Mechanism, Taraborrelli et al. (2012), ~300 reactions of ~150 species) conventionally used in our simulations. We find that MOM exhibits different sensitivity of O_x and HO_x species to reactive N loading in the troposphere (such result is typical for inter-comparisons of mechanisms from various AC-GCMs as well). In particular, comparable PD tropospheric NO_x burden results in larger O₃ and similar OH concentrations albeit lower CH₄ sink (hence longer lifetime) in MOM. Somehow counterintuitive (as OH production is rate-limited by O₃ photolysis), this result indicates that OH redistributes to areas where CH₄+OH reaction is slower (colder air). This is in line with expected larger OH reactivity due to larger set of oxygenated volatile organic compounds represented in MOM (Lelieveld et al., 2016). In the LGM conditions, however, the difference between MIM and MOM are smaller due to absent anthropogenic emissions and similarity in primary OH production. In other climate states (e.g. during deglaciation) this may be not the case, therefore we intend to perform control simulations with MOM for every chosen time slice. In the PD conditions, longer CH₄ lifetime is expected with MOM, as the adequate tropospheric O₃ abundance requires lowering of the LNO_x source. Much less important in present-day conditions, this may have a large effect on OH in the LGM. This remains to be investigated in our near-future simulations, in line with the task on calibration of lightning parameterisations in EMAC.

WP2.4 “Dust cycle” is focused on the interactive simulation of dust sources and depositions during the last deglaciation. The interactive model of dust emission, transport, and deposition as well as a modulator of the radiative forcing will be an intrinsic part of ESM simulations in WG1. In addition, the biogeochemical role of dust as a forcing for marine biogeochemistry through Aeolian transport and deposition of micro-nutrients (iron) will be explored together with WP2.1. WP2.4 work

is performed at TROPOS.

Work achieved until 2019-10-31

The ability to reproduce dust emission from different dust source types, as well as interannual variability in dust emission fluxes, atmospheric dust concentration, and deposition fluxes is challenging and crucial for understanding dust-climate feedbacks. In order to ultimately aim for a computationally efficient dust module implemented in the MPI-ESM the dust emission module from the ECHAM-HAM atmosphere-aerosol model was taken and incorporated in MPI-ESM. Dust emission depends crucially on sediment supply and availability with the latter being strongly influenced by vegetation cover of the surface. To account for changing vegetation in changing climates and its influence on dust emission the dust sources are computed online based on JSBACH land cover results (Stanelle et al., 2014). Dust emission itself is following the saltation approach by Tegen et al. (2002), ultimately based on Marticorena and Bergametti (1995) and updated to better represent the effect of soil moisture and East-Asian soil properties (Cheng et al., 2008). Dust is implemented as a single tracer representing coarse mode dust. For the sake of computational efficiency in view of the length of the PalMod simulations the dust deposition is realised as a simple lifetime approach replacing the sedimentation, dry and wet deposition routines in ECHAM-HAM. For diagnostic purposes the aerosol optical depth (AOD) of the dust is computed.

The new MPI-ESM-Dust model was run in a series of sensitivity simulations in order to find the optimal parameters that best reproduce the dust cycle in the present climate as a basis for modelling past conditions. First, the regional scaling factors for the threshold friction velocity had to be adjusted in order to achieve a reasonable dust emission scenario for present day climate conditions. The emitted dust mass was compared to the full ECHAM-HAM aerosol climate model in higher spatial resolution as well as to other model simulations performed within the AeroCom model intercomparison (Huneus et al., 2011). Second, the dust lifetime had to be constrained. This was done via a series of simulations where the emission was kept constant but the lifetime was gradually increased from 7 days to 10 days, 14 days and 20 days. The resulting aerosol optical depth of the dust was compared to AERONET station measurements of coarse mode AOD. Moreover, the surface concentration of dust was compared to AEROCE measurements at selected stations.

The final setup with the adjusted regional scaling factors and dust lifetime was then used to perform a series of time slice simulations, spanning 100 years each, of the LGM climate, the „Green Sahara“ period 10.000yr BP (10k), the end of the „Green Sahara“ and beginning of the North African desertification 5.000yr BP (5k) and the pre-industrial climate (PI).

Results

The new model emits more dust in the global annual average than the parent ECHAM-HAM model but it is well in the range of other AeroCom models. The optimal lifetime was found to be 10 days. This is a compromise between the AOD based and the dust surface concentration based results. The AOD comparison yielded the lowest bias and normalized root mean square error (NRME) at a lifetime of 14 days while the analysis of the surface concentration gave at 7 days the lowest bias and NRME.

The time slice simulations show significant differences in the emission of dust, largely governed by the vegetation cover of the respective climate (Figure 9).

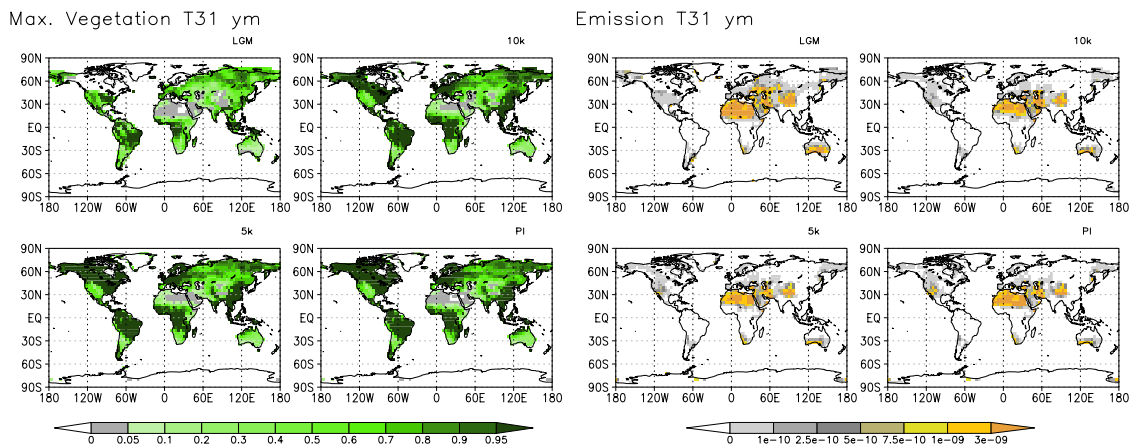


Fig. 9: Left: Simulated annual mean maximum vegetation cover of the grid cells at LGM, 10k, 5k and PI. Right: Annual mean dust emission in $\text{kg}/\text{m}^2/\text{s}$.

The LGM dust emissions are clearly enhanced compared to the pre-industrial climate, globally by a factor of 1.6, regionally up to a factor of 4 (Australia, South America). During the “Green Sahara” period (10k) the Northern African emissions are decreased by 40% compared to PI, due to the vegetation cover of the largest modern dust source. However, the vegetation in Northern Africa at 10k and 5k is rather similar, such that the dust emissions are only slightly enhanced at 5k. Most probably the desertification is delayed in the deglaciation simulation from which the restart fields were provided.

References:

- Cheng, T., Peng, Y., Feichter, J., and I. Tegen, An improvement on the dust emission scheme in the global aerosol-climate model ECHAM5-HAM, *Atmos. Chem. Phys.*, **8**, 1105–1117, doi:10.5194/acp-8-1105-2008, 2008.
- Lacroix, F., Ilyina, T., and Hartmann, J.: Oceanic CO_2 outgassing and biological production hotspots induced by pre-industrial river loads of nutrients and carbon in a global modelling approach, *Biogeosciences Discuss.*, <https://doi.org/10.5194/bg-2019-152>, in review, 2019.
- Giorgetta, M. A., et al.: Climate and carbon cycle changes from 1850 to 2100 in MPI-ESM simulations for the Coupled Model Intercomparison Project phase 5, *J. Adv. Model Earth Syst.*, **5**, 572–597, doi: [10.1002/jame.20038](https://doi.org/10.1002/jame.20038), 2013.
- Hopcroft, P. O., et al.: Understanding the glacial methane cycle, *Nat. Commun.*, **8**, 14383, doi: [10.1038/ncomms14383](https://doi.org/10.1038/ncomms14383), 2017.
- Huneus, N., Schulz, M., Balkanski, Y., Griesfeller, J., Prospero, J., Kinne, S., Bauer, S., Boucher, O., Chin, M., Dentener, F., Diehl, T., Easter, R., Fillmore, D., Ghan, S., Ginoux, P., Grini, A., Horowitz, L., Koch, D., Krol, M. C., Landing, W., Liu, X., Mahowald, N., Miller, R., Morcrette, J.-J., Myhre, G., Penner, J., Perlwitz, J., Stier, P., Takemura, T., and Zender, C. S.: Global dust model intercomparison in AeroCom phase I, *Atmos. Chem. Phys.*, **11**, 7781–7816, <https://doi.org/10.5194/acp-11-7781-2011>, 2011.
- Lelieveld, J., et al.: Global tropospheric hydroxyl distribution, budget and reactivity, *Atmos. Chem. Phys.*, **16**, 12477–12493, doi: [10.5194/acp-16-12477-2016](https://doi.org/10.5194/acp-16-12477-2016), 2016.
- Martcorena, B. and Bergametti, G.: Modeling the atmospheric dust cycle. 1. Design of a soil-derived dust emission scheme. *J. Geophys. Res.*, **100** (D8), 16.415–16.430, 1995.
- Sander, R., et al.: The community atmospheric chemistry box model CAABA/MECCA-4.0, *Geosci. Model Dev.*, **12**, 1365–1385, doi: [10.5194/gmd-12-1365-2019](https://doi.org/10.5194/gmd-12-1365-2019), 2019.
- Stanelle, T., Bey, I., Raddatz, T., Reick, C., and Tegen, I.: Anthropogenically induced changes in twentieth century mineral dust burden and the associated impact on radiative forcing, *J. Geophys. Res.*, doi:10.1002/2014JD022062, 2014.
- Taraborrelli, D., et al.: Hydroxyl radical buffered by isoprene oxidation over tropical forests, *Nat. Geosci.*, **5**, 190–193, doi: [10.1038/ngeo1405](https://doi.org/10.1038/ngeo1405), 2012.

Tegen, I., Harrison, S. P., Kohfeld, K., Prentice, I. C., Coe, M., and M. Heimann, Impact of vegetation and preferential source areas on global dust aerosol: Results from a model study, *J. Geophys. Res.*, 107(D21), 4576, doi:10.1029/2001JD000963, 2002.

Project Report 2019

Project: 1029

Project title: From the Last Interglacial to the Anthropocene:
Modeling a Complete Glacial Cycle (PalMod), WG3

Project lead:

Report Period: 1.1.2019 – 30.06.2019

1. Used resources in 2019

The standard model MPI-ESM (ie. without water isotopes diagnostics) has been updated to the version 1.2.01p1. We followed the same procedure with the isotope-enabled version of the model to be consistent. Because of this update, we had to prolongate our isotopic simulations performed in 2018 in addition to the new ones planned for 2019. In total, we ran 2700 model years, which represent around 44,000 node hours. Due to the limited computing resources allocated for this project compared to those requested initially, we tried to be cautious in the consumption of these resources or to use other projects computing time. As we work in very close collaboration with the PalMod WG1 group, and due to the lack of space in the WG3 working directory, we had the possibility to store the data in WG1 disk space.

2. Short summary of achieved results

The water cycle is a key component of the Earth's climate system. One way to document its past evolution in order to test the models for future climate projections is to use the water stable isotopes H_2^{16}O , H_2^{18}O and HDO. They are integrated of climate processes occurring in various branches of the hydrological cycle and are extremely useful to describe its past changes. Measured in the polar ice cores, the water stables isotopes (expressed hereafter in the δ notation as $\delta^{18}\text{O}$ and δD , with respect the Vienna Standard Mean Ocean Water standard V-SMOW) are used for past temperature reconstructions over the past glacial-interglacial cycles. In continental speleothems, they can be related to the past amount of precipitation. In marine sediments, the water isotope concentrations give access to the water mass changes. The simulation of the water isotope bodies in a coupled GCM is extremely powerful as it allows a direct model-data comparison for different climate periods. This is important for testing the hydrological cycle in the models and for better explaining fundamental links between the water cycle and the climate variability.

First, we have prolonged by 500 model years our 2 equilibrium simulations under pre-industrial (PI) and mid-Holocene (6k) conditions with the isotope-enabled version of MPI-ESM (version 1.2.01p1), called hereafter MPI-ESM-wiso. A manuscript evaluating the model under PI conditions and the isotopes-climate relationships for different warm climatic periods has been accepted for publication in *Climate of The Past* (PalMod Special Issue): <https://www.clim-past-discuss.net/cp-2019-72/>. We summarize this study below. The Figure 1 shows the global distribution of annual mean $\delta^{18}\text{O}$ values in precipitation ($\delta^{18}\text{O}_p$) under pre-industrial conditions as simulated by MPI-ESM-wiso. The comparison with the isotopic data (observations from GNIP stations (IAEA), ice core records and SISAL speleothems records dataset) shows a very good agreement with a model-data slope of 0.87 (1 being the perfect

fit) and a root mean squared error (RMSE) of 2.26 ‰. The modelled $\delta^{18}\text{O}$ -temperature gradient ($0.63 \text{ ‰}/^\circ\text{C}$; $r^2=0.97$) is also very close of the observed one ($0.66 \text{ ‰}/^\circ\text{C}$; $r^2=0.95$). This represents a slight improvement compared to the ECHAM5/MPIOM model enabled with water isotopes.

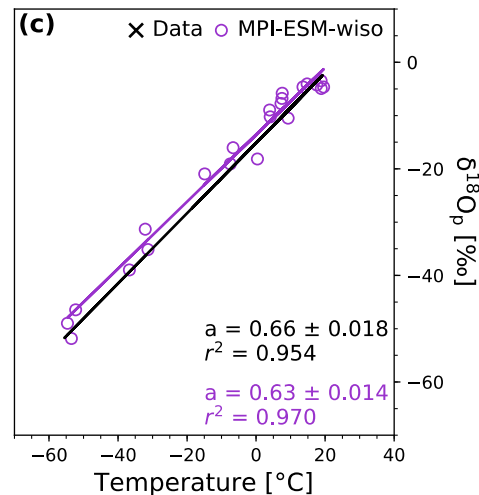
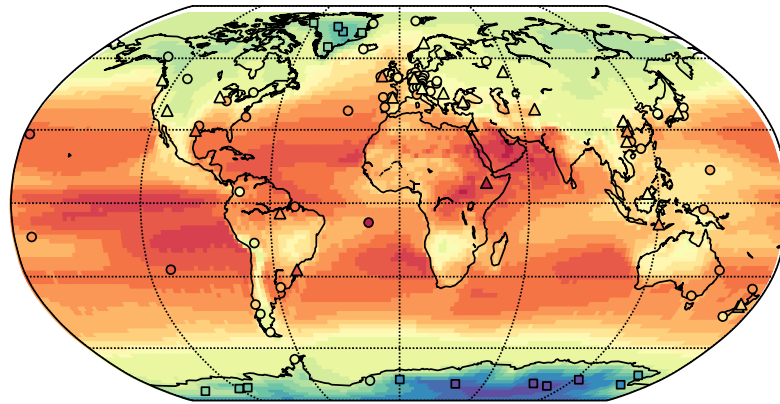


Figure 1: (a) Global distribution of simulated (background pattern) and observed (colored markers, see text for details) annual mean $\delta^{18}\text{O}_p$ values in precipitation under PI conditions. The data consist of 70 GNIP stations (circles), 15 ice core records (squares) and 33 speleothem records (triangles). (b) Modelled vs. observed annual mean $\delta^{18}\text{O}_p$ at the different GNIP, speleothem, and ice core sites. (c) Observed (black crosses) and modelled (purple circles) spatial $\delta^{18}\text{O}_p$ - T relationship for the sites where the observed annual mean temperatures are below $+20^\circ\text{C}$. The linear fits for the observed and modelled values are drawn as black and red lines respectively. For both (b) and (c), the gradients of the linear regression fits are given in the legends.

By simulating different time periods with an isotope-enabled model, it is possible to study the changes in $\delta^{18}\text{O}$ between two climatic periods and its relationship with climatic parameter as temperature, precipitation or salinity. In our paper, the evaluation of these changes between mid-Holocene period and pre-industrial allows to examine the forced response to orbital and greenhouse gas forcing. The Figure 2 shows the modelled changes in $\delta^{18}\text{O}_p$ between 6k and PI and a comparison with some observations from ice cores and speleothem records. At the high latitudes, the water isotope variations are mainly influenced by the changes in temperature while the 6k-PI $\delta^{18}\text{O}_p$ anomalies at lower latitudes are mainly driven by the changes in the amount of precipitation, especially over the Pacific Ocean on the Asian coast and over the East Indian Ocean. The model results agree relatively well with the available data. The largest deviations are found for two speleothems located in Ethiopia and in the

Great Basin of western North America. These discrepancies likely reflect an insufficient amplification of precipitation rate (or its wrong location) over eastern Africa and a too weak increase of temperature over Northeast America during the mid-Holocene period. More generally, the amplitude of the modeled $\delta^{18}\text{O}_p$ changes at speleothem sites is underestimated by MPI-ESM-iso. This is likely related to the underestimation by the model of the 6k changes in climate variables like temperature and precipitation rate, as already noticed in previous model studies

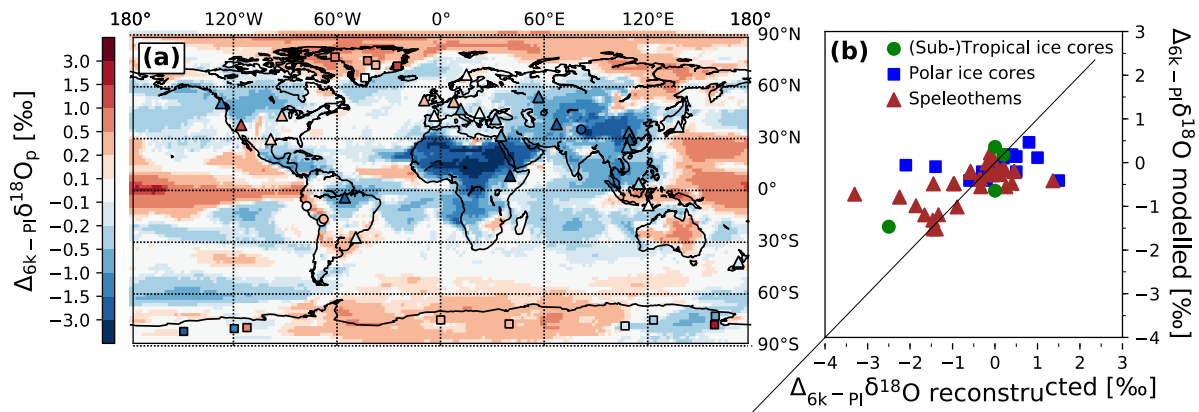


Figure 2: (a) Simulated global pattern of annual mean $\delta^{18}\text{O}_p$ changes in precipitation between the mid-Holocene and PI climate and comparison with reconstructed $\delta^{18}\text{O}$ changes in polar (squares) and (sub-)tropical (dots) ice cores and in calcite speleothems (triangles). (b) Reconstructed $\delta^{18}\text{O}$ changes from ice cores and speleothems vs. simulated 6k-PI $\delta^{18}\text{O}$ anomalies at the same location.

Then, we also performed a simulation for the Last InterGlacial period (LIG, 127 ka), following the PMIP4 protocol. For reaching a quasi-equilibrium state with the water isotopes, we let run the model for 1500 model years and present here an average of the last 150 model years (Figure 3). The temperature during LIG is higher over the high latitudes during the LIG compared to PI. In boreal summer (mean of June, July, and August months), the increase in temperature compared to PI state can be more than 4°C over the northern hemisphere land. The monsoons over Africa and Asia are also highly enhanced during boreal summer. All of these patterns influence the LIG-PI $\delta^{18}\text{O}_p$ anomalies with higher values over Greenland and Antarctica due to the higher temperatures, and lower $\delta^{18}\text{O}_p$ values over Northern Africa, India and China because of the precipitation amount effect. These model results need to be compared to available isotopic observations from ice cores and speleothems and will be used for providing isotopic PMIP maps based on the SISAL speleothems dataset.

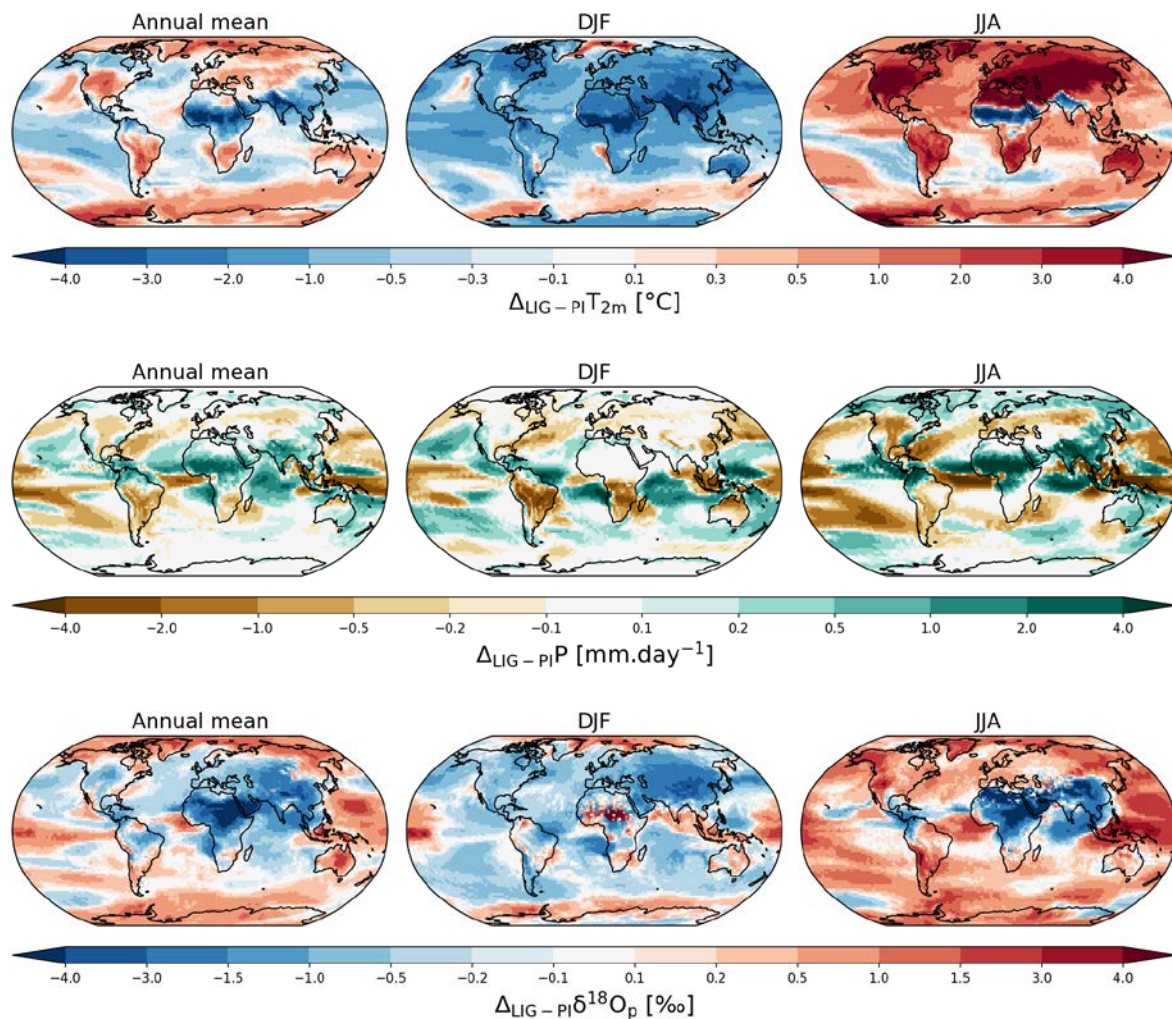


Figure 3: Simulated annual, boreal winter (DJF) and boreal summer (JJA) changes in 2m-temperature (first row), precipitation (second row), and $\delta^{18}\text{O}_p$ (last row) between LIG and PI.

Finally, we extended by additional 200 model years our PI simulation presented in Figure 1 to investigate the modelled temperature- $\delta^{18}\text{O}_p$ temporal correlation over East Antarctic ice core sites. This ongoing work is in collaboration with Thomas Münch and Thomas Laepple from the Alfred Wegener Institute in Potsdam, and who are also involved in the PalMod project.

Concerning the promised hosing experiments, a new LGM run (Last Glacial Maximum, 21 ka) with the updated version of MPI-ESM had to be performed first. A MPI-ESM simulation without isotopes is ongoing and we hope to run the LGM simulation with isotopes diagnostics by the end of the year with remaining computing time resources.

Report of works done on mistral from WP3 TP2 FUB in 2019

In **WP-3.3 TP2 (FUB)**, after analysis of the simulations done in 2018, we decided to set up new sets of simulations to study the behaviour of the model under different forcing and its uncertainty (e.g. structural uncertainty). We check the spatial sensitivity of model parameters to different forcings; test whether some specific process leads to changes in the spatial patterns of near surface temperature anomalies. We aim to get closer to evidence from pollen data; and finally we want to characterize how much the model spread changes following changes in the forcings. To have an idea on the structural stability of the model we set-up two sets of simulations for Pre-industrial and mid-Holocene. We plan to publish the results in the next year. The simulations are based on MPI-ESM runs of pre-industrial and mid-Holocene climate conditions (AWI). We tested different parametrization schemes and parametrization values. The parameters that were perturbed were based on the work conducted at ETH Zürich. We tested the most sensitive parameters of the model over Europe (Bellprat and Doblas-Reyes, 2016, Bellprat et al., 2015 and personal communication with Soerland and Schär). On top of that, we perturbed some physical options like albedo, forest fraction, soil heat conductivity, ratio of soil moisture and soil-ice .

Finally, we expanded the Data Assimilation (DA) experience with the better characterization of the model error (Fig.1). First results, show that the impact of the boundaries are larger than other parameters and the CCLM is influenced mostly by the GCM itself than other forcings. The changes in the spread of the model simulation using the two different GCM simulations (PI and mid-Holocene) is very small, which indicates a good stability of the RCM using different GCMs.

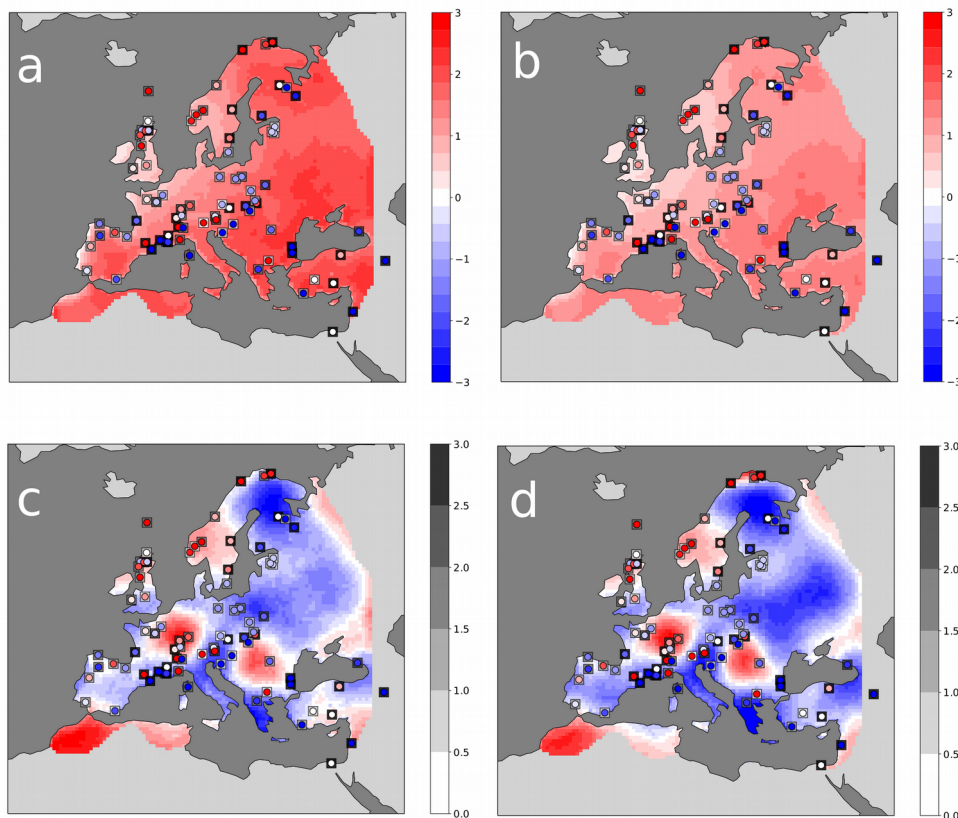


Figure 1: An example of mid-Holocene simulations with two different configurations in which the parameters are perturbed: Summer Temperature anomalies (mid-Holocene minus PI) for a) case 1 and b) case 2. c) and d) are the corresponding analysis (using offline DA). Circles indicate the test sets of reconstructions which are not assimilated. Gray boxes show the uncertainty in the reconstructions.

Simulations:

COSMO-CLM 5.00

- 26 years x 15 CCLM simulations for Pre-Industrial over Europe
- 26 years x 15 CCLM simulations for mid-Holocene over Europe

Resource utilization used till 15.10.2018 :

- Mistral computer time [node hours]	:	9502
- Lustre work [GiB]	:	8160
- HPSS arch [GiB]	:	58091

Reference:

Bellprat, O., and F. Doblas-Reyes (2016), Attribution of extreme weather and climate events overestimated by unreliable climate simulations, *Geophys. Res. Lett.*, 43, doi:10.1002/2015GL067189.

Bellprat, Omar & Kotlarski, Sven & Lüthi, Daniel & Elía, Ramón & Frigon, Anne & Laprise, René & Schär, Christoph. (2015). Objective Calibration of Regional Climate Models: Application over Europe and North America. *Journal of Climate*. 29. 151211135749001. 10.1175/JCLI-D-15-0302.1.

Project: **993**
Project title: **PalMod WG4**
Project lead: **Hendryk Bockelmann**
Report period: **2019-01-01 to 2019-12-31**

Work Package 4.2

We further post-processed and analysed the data produced in PalMod phase I – especially data from 2018. Hence, no additional compute-time was used. The preparation of the data for archiving and final publication is still ongoing and we expect to finalise it in early 2020 with the support of the Cross Cutting Activities group in PalMod phase II.

Work Package 4.3

In order to develop and evaluate the usability of parallel-in-time methods for climate models such as ECHAM6 and FESOM2, we prepared the basic method based on a shallow-water model. These experiments were not performed on computing resources at DKRZ.

Work Package 4.4

TP1

Many AMIP-type experiments were designed and performed during the implementation and verification of the asynchronous radiation scheme in ECHAM6. In this scheme, the radiation component was made isolated from the main model in a separate namespace and re-integrated back to the code as an external component, operating at the sequential, synchronous and asynchronous modes. The sequential mode resembles the classical radiation scheme in ECHAM6, but the coupling fields between the radiation component and the main model are explicitly exchanged through the shared memory. In addition, the synchronous mode resembles the classical radiation scheme except for the fact that now the coupling fields are exchanged through MPI communications using the YAXT library (Behrens et al, 2018). The communication costs between the external radiation and the main model were measured and turned out to be negligible in comparison to the radiation calculation itself (almost less than 0.4% - Figure 1). Both modes using the external radiation – sequential and synchronous - still generate bit-identical results in comparison to the classical ECHAM6 at the sequential mode.

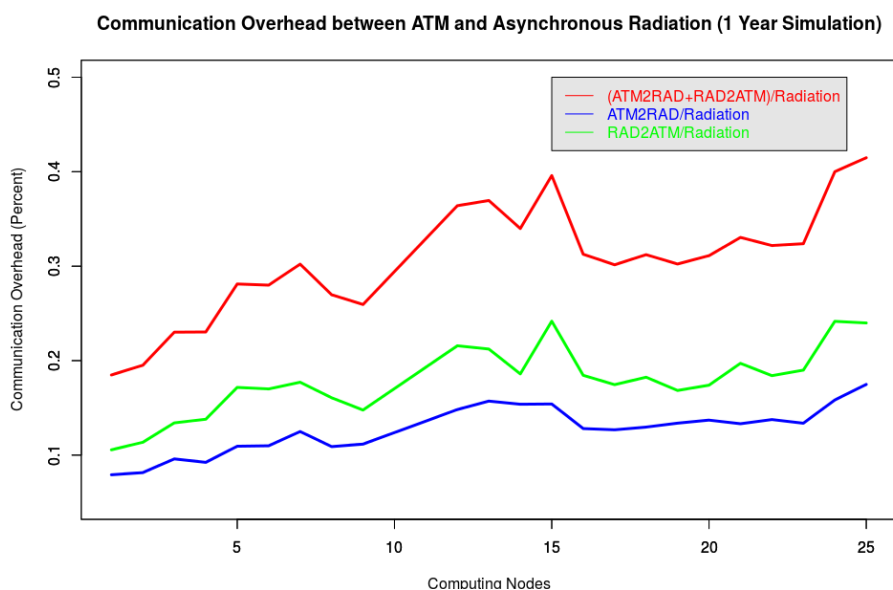


Figure 1: Communication overhead between the asynchronous radiation and atmosphere in ECHAM6.

Finally, we conducted the same set of AMIP-type experiments to evaluate the speedup of the asynchronous radiation scheme in respect to the classical approach in ECHAM6. For this study, simulations at CR (T31) were used at different scaling setups and the scaling curves were extracted. As Figure 2 shows, a maximum speedup of 1.7 was achieved.

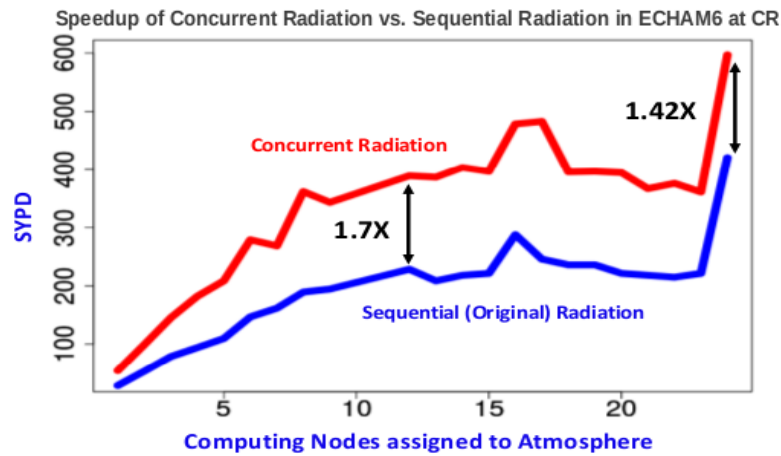


Figure 2: Speedup of the asynchronous radiation scheme vs. sequential radiation scheme in ECHAM6.

To evaluate the differences and possible improvements in the simulated mean climate and its variability between the sequential and asynchronous radiation scheme, two sets of AMIP-type (Atmospheric Model Intercomparison Project) simulations are conducted with the ECHAM6 at CR (course resolution) and LR (low resolution) settings, respectively. Each set consists of six experiments: two simulations using the sequential radiation scheme with the default and 1-hour radiation calculation frequency (hereafter named as Seq_{2hr} and Seq_{1hr}); four simulations using the asynchronous radiation scheme with 2-hour, 1.5-hour, 1-hour and 0.75-hour radiation calculation frequency (hereafter named as Asy_{2hr} , $Asy_{1.5hr}$, Asy_{1hr} and $Asy_{0.75hr}$). For the AMIP-type experiments, sea surface temperature, sea ice, ozone and greenhouse gas forcing are prescribed. Each simulation is integrated from the year 1960 to the year 2013. For the experiments with CR setting, monthly mean output from 1980 to 2013 is taken for scientific evaluation. In contrast, the daily mean output with LR setting from 1980 to 2013 is evaluated.

Regarding to the simulated mean climate, the magnitude and spatial patterns of the errors in the 2m-air-temperature, precipitation, cloud radiative forcing (a measure of cloud feedback), zonal mean thermal structure and zonal mean zonal winds relative to the observational and reanalysis data are evaluated. Generally, there are minor differences between the simulations with the sequential and asynchronous radiation scheme at both CR and LR settings. Specifically, Asy_{1hr} agrees reasonably well with the original model at the default setting (Seq_{2hr}), while the discrepancies between Seq_{2hr} and other experiments using the asynchronous scheme are relatively larger.

Additionally, the simulated annual and inter-annual climate variability are assessed. Special attention is given to the atmospheric teleconnection patterns associated with the ENSO (El Niño-Southern Oscillation), NAM (Northern Annual Mode) and SAM (Southern Annual Mode). In terms of the teleconnection patterns for the ENSO and NAM, Asy_{1hr} exhibits better agreement with the reanalysis data and the original model than other simulations. Moreover, the simulated teleconnection pattern for the SAM is significantly improved in Asy_{1hr} relative to the original model at CR settings (Figure 3). Shorter time-scale climate variability, such as the Madden-Julian Oscillation, is evaluated with the set of simulations at LR setting. Consistent with previous results, Asy_{1hr} differs slightly from the Seq_{2hr} , which agrees reasonably well with the reanalysis data.

We conclude from the AMIP-type experiments that the asynchronous radiation scheme with 1-hour radiation calculation frequency exhibits negligible discrepancies from the original model. Additionally, the simulated atmospheric teleconnections associated with the SAM is significantly improved with the asynchronous scheme.

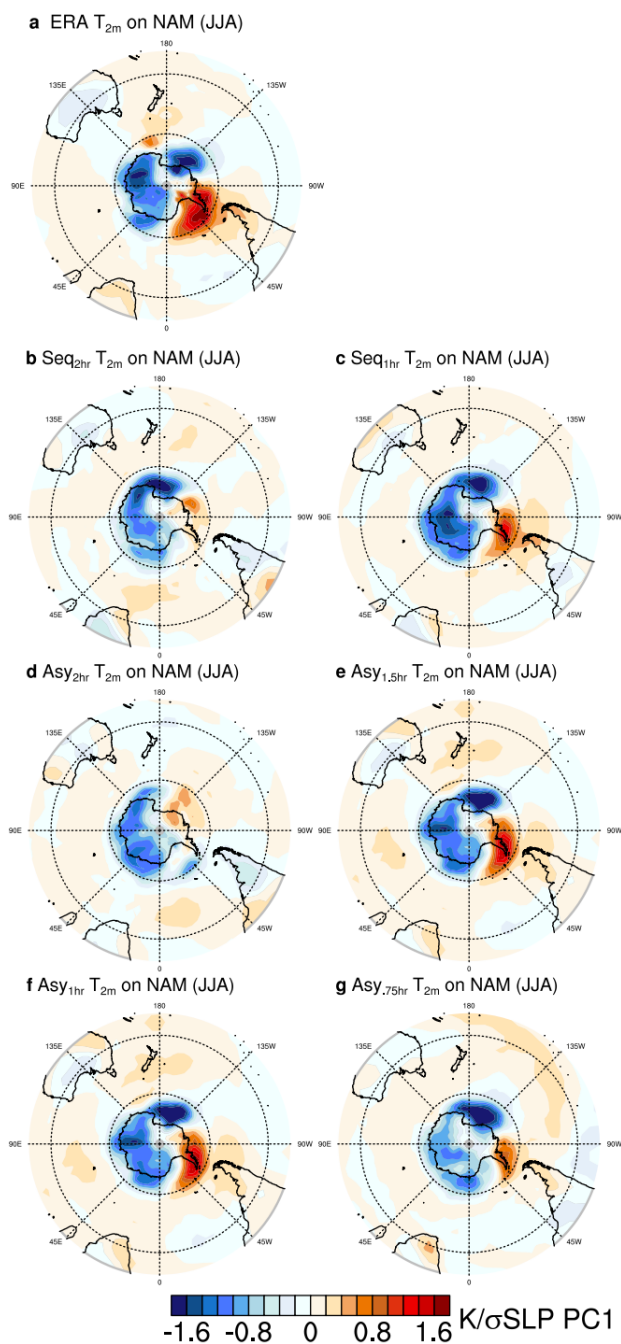


Figure 3: Regression of JJA (June-July-August) 2m-air-temperature anomalies on the normalized time series of PC1 corresponding to the EOF1 of JJA SLP (sea level pressure) for (a) the ERA-Interim, (b) Seq_{2hr}, (c) Seq_{1hr}, (d) Asy_{2hr}, (e) Asy_{1.5hr}, (f) Asy_{1hr} and (g) Asy_{0.75hr}.

TP2

The implementation of single precision arithmetic inside ECHAM6 radiation required wide investigations. Model output as well as time performance had to be evaluated. A broad amount of tests has been performed by the use of the granted resources. A wide amount of modified models has been tested to evaluate the circumstances where single precision caused crashes or inconsistent model output.

The obtained speedup has been proven to be highly dependent on several parameters (in particular nprma) that had to be bulky tested. Results of these tests showed overall time gain as well as consistent model output. Resources used are also leading to the draft of a paper on the properties of the model with single precision radiation which is currently being prepared for publication.

TP3

For climate simulations on glacial timescales, MPIOM has been adjusted to handle changes in ocean topography automatically. In this reporting period, we finalised the automatic adjustment of the biogeochemical model HAMOCC to changes in the ocean topography. For tracers of the water column we follow the same strategy as for salinity in MPIOM. Changes in the ocean topography also include drying and flooding of individual grid cells. For HAMOCC, this requires an adjustment of the sediment module. In case of flooding, we assume an *empty* sediment, i.e. the local sediment column is filled only with sand in a solid constituent. The pore water is filled by water tracer concentrations from the overlying ocean. In case of drying, we transfer the pore water tracer inventory to the water column. Solid constituents at these locations are accumulated in an extra file to keep track of mass loss. The full system is mass conserving within computational precision.

Changes of the land-sea mask could also include flooding of land points covered by vegetation. We distribute the different carbon pools from JSBACH to the water column and the sediment. Short living land carbon, such as leaves or non woody litter, are assumed to be respired instantaneously and the carbon is emitted to the atmosphere. Woody litter and humus from above ground (below ground) enter the water column (sediment) as terrestrial organic matter. These terrestrial organic components are treated similar as organic matter of marine origin with respect to horizontal displacement and remineralization processes. However, they come with their own carbon and nutrient composition (following Goll et al., 2012) and remineralization time constants (5-10 years). The standing wood inventory is transfer to a locally fixed organic matter pool at the water-sediment interface. A remineralization time constant of 100 years is assumed for this component. Until the end of the year, we finalise a full deglaciation simulation based on the GLAC-1D ice sheet reconstruction.

A second focus of this reporting period was to develop a coral module for the coarse resolution MPI-ESM setup. Corals grow in distinct water depth and, thus, follow sea level rise. One major obstacle of the representation of corals in coarse resolution models is the lack of shallow areas being suitable habitats. We developed a method to determine the fraction of shallow regions within a grid cell based on the high-resolution topography. Combined equations describing growth depending on photosynthesis and calcification depending on the aragonite saturation state of the ambient water govern coral reef inventories. Simulated present day distribution catches the regions of observed coral reefs (Figure 4). However, further development and testing are needed to include coral reef migration with sea level rise and calcite dissolution or coral destruction by predators such as fish or chemical borers.

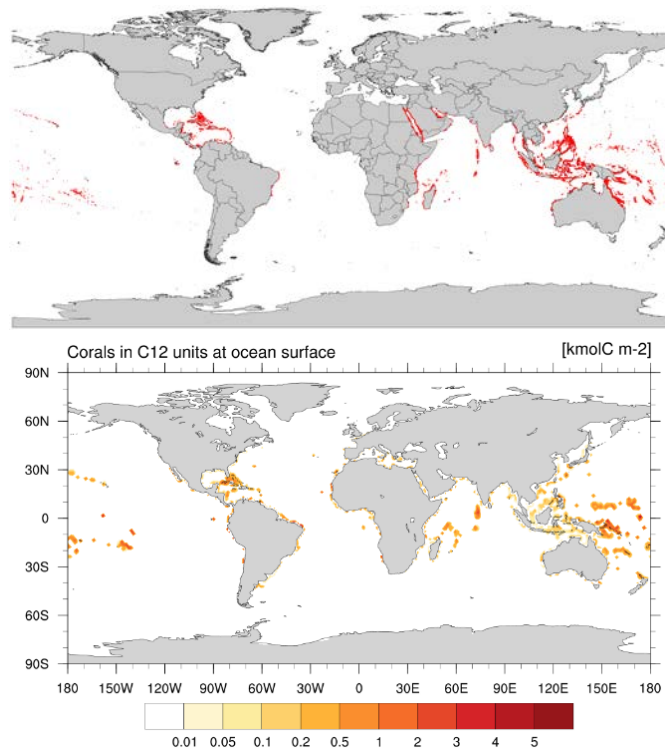


Figure 4: Present day coral reef distribution (red areas in top panel from Teh et al., 2013) and present day coral reef distribution simulated with stand-alone MPIOM/HAMOCC (bottom panel, given in kmol C m⁻²)

TP4

The evaluation of AMR (adaptive mesh refinement) for tracer transport on dust simulation in ECHAM-HAMMOZ was mainly done interactively on data produced while the whole first phase of the PalMod project. Therefore, this subproject did not use a noticeable part of the granted resources. We published one conference paper already in 2018 and new publication is currently under preparation.

References:

Behrens, J., Biercamp, J., Bockelmann, H., and Neumann, P. Increasing parallelism in climate models via additional component concurrency. 2018 IEEE 14th International Conference on e-Science, pp. 271–271, 2018

Chen, Y., Simon, K., and Behrens J., 2018, June. Enabling Adaptive Mesh Refinement for Single Components in ECHAM6. In International Conference on Computational Science (pp. 56-58). Springer, Cham.

Goll, D. S. et al. (2012) Nutrient limitation reduces land carbon uptake in simulations with a model of combined carbon, nitrogen and phosphorus cycling, *Biogeosciences*, doi: 10.5194/bg-9-3547-

Teh L.S.L. et al. (2013) A Global Estimate of the Number of Coral Reef Fishers. *PLoS ONE* doi: 10.1371/journal.pone.00653972012